

UCLA

UCLA Previously Published Works

Title

Experimental study on novel biodegradable Zn-Fe-Si alloys.

Permalink

<https://escholarship.org/uc/item/4qd1z5s2>

Journal

Journal of Biomedical Materials Research Part B: Applied Biomaterials, 110(10)

Authors

Guan, Zeyi
Pan, Shuaihang
Liu, Jingke
et al.

Publication Date

2022-10-01

DOI

10.1002/jbm.b.35075

Peer reviewed



HHS Public Access

Author manuscript

J Biomed Mater Res B Appl Biomater. Author manuscript; available in PMC 2023 October 01.

Published in final edited form as:

J Biomed Mater Res B Appl Biomater. 2022 October ; 110(10): 2266–2275. doi:10.1002/jbm.b.35075.

Experimental Study on Novel Biodegradable Zn-Fe-Si Alloys

Yuxin Zeng^a, Zeyi Guan^a, Chase S. Linsley^b, Shuaihang Pan^a, Jingke Liu^a, Benjamin M. Wu^{b,c,d,e}, Xiaochun Li^{a,c,*}

^aDepartment of Mechanical and Aerospace Engineering, Samueli School of Engineering, University of California, Los Angeles, CA 90095, USA

^bDepartment of Bioengineering, Samueli School of Engineering, University of California, Los Angeles, CA 90095, USA

^cDepartment of Materials Science and Engineering, Samueli School of Engineering, University of California, Los Angeles, CA 90095, USA

^dDivision of Advanced Prosthodontics, School of Dentistry, University of California, Los Angeles, CA 90095, USA

^eDepartment of Orthopedic Surgery, David Geffen School of Medicine, University of California, Los Angeles, CA 90095, USA

Abstract

Bioabsorbable metals are increasingly attracting attention for their potential use as materials for degradable implant devices. Zinc (Zn) alloys have shown great promises due to their good biocompatibility and favorable degradation rate. However, it has been difficult to maintain an appropriate balance among strength, ductility, biocompatibility, and corrosion rate for Zn alloys historically. In this study, the microstructure, chemical composition, mechanical properties, biocompatibility, and corrosion rate of a new ternary zinc-iron-silicon (Zn-Fe-Si) alloy system was studied as a novel material for potential biodegradable implant applications. The results demonstrated that the *in-situ* formed Fe-Si intermetallic phases enhanced the mechanical strength of the material while maintaining a favorable ductility. With Fe-Si reinforcements, the microhardness of the Zn alloys was enhanced by up to 43%. The tensile strength was increased by up to 76% while elongation to failure remained above 30%. Indirect cytotoxicity testing showed the Zn-Fe-Si system had good biocompatibility. Immersion testing revealed the corrosion rate of Zn-Fe-Si system was not statistically different from pure Zn. To understand the underlying phase formation mechanism, the reaction process in this ternary system during the processing was also studied via phase evolution and Gibbs free energy analysis. The results suggest the Zn-Fe-Si ternary system is a promising new material for bioabsorbable metallic medical devices.

Keywords

Zn-Fe-Si alloys; *in-situ* formed intermetallic; biodegradable; mechanical properties; biocompatibility

*Corresponding Author, xcli@seas.ucla.edu.

1 INTRODUCTION

Implants are an important tool in the surgeon's arsenal that can be used for diagnostic, therapeutic, and regenerative applications [1]. Most implantable medical devices are permanent, and either require a second surgery to remove or have been designed to integrate with the host tissue in a stable manner (e.g. bioinert). However, long-term complications are not uncommon [2][3][4], and permanent implants are usually not suitable for children since their size is fixed and cannot grow with the child. Biodegradable metals have soluble corrosion products and gradually dissolve away *in vivo* upon tissue healing [5]. There are several load-bearing clinical applications that would benefit from the development of safe and efficacious biodegradable metallic implant materials, such as bone fixation devices, barrier membranes, surgical staples, suture wires, and cardiovascular stents. The development of a metallic bioresorbable stent (BRS) would revolutionize the treatment of aortic coarctation and pulmonary stenosis in pediatric patients since these patients could be treated in a minimally invasive fashion instead of requiring open chest surgery [6]. As such, there have been many studies in the last decade dedicated to the development of alloys suitable for BRS applications.

Currently, the three most studied metals for BRS are magnesium (Mg), iron (Fe), and zinc (Zn). Mg-based stents are furthest along the clinical development pipeline and have been clinically tested for coronary artery diseases [7][8][9][10][11]. However, there are limitations including a fast degradation rate [12], formation of hydrogen gas [13], and restenosis, possibly due to the rapid loss of mechanical integrity [14]. Fe has also been widely studied as a BRS material due to its excellent mechanical properties and slower corrosion rate [15], but the corrosion products have caused inflammation in preclinical studies [16][17]. Zn-based materials have recently emerged as an ideal candidate for BRS because Zn offers excellent biocompatibility, an ideal corrosion rate, and great ductility [18]. However, pure Zn has relatively low mechanical strength. As such, several Zn alloys have been developed to satisfy mechanical requirements for vascular stents, including Zn-aluminum (Zn-Al) [19], Zn-Fe [20], Zn-Mg [21] [22], and Zn-strontium (Zn-Sr) [22]. A major challenge for Zn alloys meant to be used as a BRS material is to achieve an optimal combination of mechanical strength, ductility, biocompatibility, and corrosion rate. Recently, Zn nanocomposites have shown great potential in overcoming this challenge. Zn-based nanocomposites can provide high strength and elongation at failure above 30% without compromising the corrosion rate of pure Zn [23][24][25][26][27]. Specifically, the benefits of nano- and micro-sized metallic ceramic or intermetallic particles come from Orowan strengthening and grain growth restriction via Zener pinning effect. However, *ex situ* synthesis of these particles is limited by the poor solubility of ceramic particles in molten metals. Also, the large lattice mismatch between the matrix and ceramic particle means porosity and particle coarsening can be introduced during *ex situ* synthesis.

In situ synthesis of micro-sized intermetallic phases eliminates the limitations associated with *ex situ* synthesis methods, and proposes a better manufacturing method for high-quality biomedical devices. *In situ* formed Fe-Si intermetallic phase may be a good choice for strengthening Zn because the hard and stable Fe-Si intermetallic should be similar to other well-studied ceramic particles and contribute to the property enhancement of the

matrix. Also, both Fe and Si are key minerals found in the body that are important for oxygen transport by hemoglobin and strengthening connective tissues, bones, and joints, respectively [28][29]. Furthermore, this ternary system was previously studied briefly by powder metallurgy to synthesize different Zn-Fe-Si alloy compositions at 450°C [30]. However, the energy-intensive powder metallurgy synthesis limited the manufacturing efficiency, plus no mechanical testing was performed in that paper.

In this study, we used a more time- and energy-efficient method of liquid metallurgy to introduce micro intermetallic phases to strengthen the Zn matrix. Based on the available phase diagram limited at only 450°C [30], Fe and Si were first incorporated into molten Zn at 750°C and then held at 825°C for dissolution. The resulting microstructure, mechanical properties, indirect cytocompatibility, and corrosion behavior of the resultant Zn-Fe-Si alloys were studied. The results showed that the microhardness and tensile strength of the ternary alloy were significantly greater than pure Zn. Also, elongation to failure was greater than 30% for all samples while there was little loss in cell viability during indirect cytotoxicity testing. Furthermore, there was no significant difference in the corrosion rate of the Zn-Fe-Si alloys compared to pure Zn. These results suggest that Zn-Fe-Si alloy is a promising material for BRS applications that warrants further research and development.

2 Materials and methods

2.1 Fabrication process

High purity Zn ingots (purity 99.995%, Rotometal), silicon metal powder (purity 99+%, 325 mesh in diameter, Atlantic Equipment Engineers), and iron granules (purity 99.98%, 1-2 mm in diameter, Beantown Chemical) were used to fabricate the alloys. A salt mixture of potassium chloride (KCl) and sodium chloride (NaCl) (volume ratio 1:1) was first melted at 750°C in a clean graphite crucible (see Fig. 1). Pure Zn was then added and melted under an inert atmosphere (Ar) followed by the addition of Fe granules and stirring until the granules were completely dissolved. The molten salts protected the molten zinc from oxidation and evaporation during mixing. Silicon powders were then added to the melt at 825±25 °C under stirring. After Si dissolution and salt removal, the molten Zn alloys were cast into a graphite plate mold and then air cooled to room temperature. The cast plate was then hot rolled at 200°C. Fig. 1 shows the detailed fabrication process.

2.2 Composition characterization

Inductively coupled plasma-mass spectrometer (ICP-MS) on a NexION 2000 model (PerkinElmer) was used to determine the final Zn, Fe, and Si content in the alloys. Hot-rolled Zn-Fe-Si alloys were cut into small pieces of size $\sim 1 \times 1 \text{ mm}^2$, and aqua regia was used to extract all three elements at room temperature.

2.3 Microstructural characterization

Zn-Fe-Si alloy samples were prepared by mechanical grinding with SiC sandpaper up to 1200 grit and polishing with alumina nanoparticle solution. The surface was then cleaned with DI water and blow dried by air gun. Microstructure characterization was performed on a scanning electron microscopy (ZEISS Supra 40VP SEM with 12kV acceleration voltage),

and X-ray diffraction (XRD; Panalytical Pro) with Cu K α radiation under standardized 40kV accelerating voltage. The step size was 0.05° with a scanning speed of 2°/min.

2.4 Mechanical testing

Microhardness test was performed on an LM 800AT microhardness tester using a load of 200gf with a 10s dwell time. Tensile testing specimens with a gage length and width of 7.5 mm and 3 mm respectively (ASTM E8/E8M standard sub-size) were fabricated by electrical discharge machining (EDM). Tensile tests were performed using an Instron ElectroPlus E1000 at a strain rate of 2 mm/min.

2.5 Cell Culture

Pooled human umbilical vein endothelial cells (HUVEC; Lonza) were cultured in Endothelial Cell Growth Medium-2 (EGM-2; Lonza) that contained hydrocortisone, fibroblast growth factor (hFGF-B), vascular endothelial growth factor (VEGF), insulin-like growth factor (R3-IGF-1), ascorbic acid, epidermal growth factor (hEGF), GA-1000 (gentamicin, amphotericin-B), heparin, 2% fetal bovine serum (FBS) (Bulletkit, Lonza), with 100 IU/mL penicillin, and 100 μ g/mL streptomycin. Cells were maintained in a humidified incubator at 37°C with 5% CO₂. HUVECs were passaged at 70-80% confluence up until adequate cell numbers were obtained for the study (< passage 10). The cells were then seeded (10,000 cells/well) in the wells of sterile 96-well plates (Costar), and maintained in a humidified incubator at 37°C with 5% CO₂ for 24 hr.

2.6 Indirect cytotoxicity assay

Square-shaped Zn-Fe-Si specimens were sterilized with 70% ethanol for >1 hr and subsequently rinsed with sterile phosphate buffer solution three times. Extract preparation for *in vitro* cytotoxicity testing closely followed ISO 10993 standard parts 5 and 12. Briefly, each of the testing samples was soaked in cell culture medium for 72 hrs in a humidified incubator at 37 °C. The surface area/volume ratio was 1.25 cm² · mL⁻¹. Post-incubation, the extracts were diluted (1:15) using fresh cell culture medium. At the time of testing, the culture medium for the cells seeded in 96-well plates (10,000 cells/well) was replaced by the sample extracts and the cells were incubated for 24 hrs and 72 hrs. Cells cultured with complete medium without any extract served as the control. At each time point, 10 μ L of the 3-(4,5-Dimethylthiazol-2-yl)-2,5-Diphenyltetrazolium Bromide (MTT) solution (5 mg/ml; BioVision) was added to each well, and subsequently incubated for an additional 4 hrs at 37 °C with 5% CO₂. Following incubation, the medium was carefully removed and 100 μ L MTT solvent solution (1:1 dimethyl sulfoxide and isopropanol) was added to each well. The plate was incubated for 15 min at room temperature and the absorbance was read at 570 nm.

2.7 Immersion Testing

Immersion tests were carried out as previously described. Briefly, each specimen was mechanically polished with SiC abrasive papers up to 1200 grit. The surfaces were cleaned with acetone followed by nanopure water in an ultrasound bath for 10 min. The immersion solution was oxygenated. At the time of testing, the specimen was immersed in 0.9% NaCl solution and kept at 37 °C without stirring, and at each time point (days 1, 4, 7, 11, and

14), aliquots of the immersion medium were collected. Afterwards, the immersion medium was completely replaced with fresh solution to mimic sink conditions. ASTM G31 standard recommends the surface area to volume ratio be a minimum of $0.2 \text{ mL} \cdot \text{mm}^{-2}$. Aliquots were filtered (0.22 μm polyvinylidene difluoride membrane) and acidified with nitric acid (final concentration = 5% v/v nitric acid). The ion concentrations of Zn, Fe, and Si in the immersion medium were measured using ICP-MS (PerkinElmer).

2.8 Statistical analysis

All statistical analyses were performed using R statistical software. For mechanical properties, one-way ANOVA tests for microhardness, tensile strength, and ductility were performed with the composition as the focused independent variable. For the microhardness, UTS, YS, and ductility, $p < 0.05$ was tested for significant difference among the three groups. For cell indirect cytotoxicity tests and immersion tests, two-way ANOVA with Tukey's multiple comparisons test was used. The normality and homogeneity of variances were measured prior to statistical tests. Here, $p < 0.05$ was also tested for significant differences among the groups.

3 Results and discussion

3.1 Chemical composition

The data from the ICP-MS analysis was used to convert the Si and Fe concentrations to atomic percentage (Table 1). The obtained Zn-Fe-Si compositions were Zn-2.723 at. % Fe-1.228 at. % Si (hereinafter, Zn-3Fe-1Si) and Zn-6.365 at. % Fe-5.566 at. % Si (hereinafter, Zn-6Fe-6Si), respectively.

3.2 Microstructure and phase identification

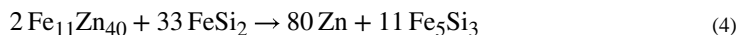
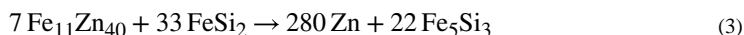
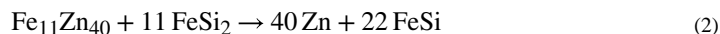
SEM was performed on both samples to investigate the dispersion of the intermetallic microphase (Fig. 2). For the Zn-3Fe-1Si sample, the resulting microstructure is shown in Fig. 2(a), (b), (e), and (f). The bright phase represents the Zn matrix and the relatively darker phase is the Fe-Si intermetallic phase (Fig. 2(b), yellow square), while the darkest phase represents Si particles (Fig. 2(b), red square). The microstructure of the Zn-6Fe-6Si sample is shown in Fig. 2(c), (d), and (g). The density of the Fe-Si intermetallic phase increases with the addition of more Fe and Si, while little-to-no Si particles were observed in this sample. The size of the Fe-Si intermetallic phase in both samples is about $10 \mu\text{m}$ (Fig. 2(e) and (g)).

XRD was performed to semi-quantitatively characterize the phases formed in the Zn-Fe-Si alloy samples (Fig. 3). Within the diffraction angles of $20^\circ - 60^\circ$, the Fe-Si intermetallic phase FeSi_2 was observed in the Zn-3Fe-1Si sample, as well as the Zn-Fe intermetallic phase $\text{Fe}_{11}\text{Zn}_{40}$. In the Zn-6Fe-6Si sample, different Fe-Si phases were observed – FeSi and Fe_5Si_3 , while there was no Zn-Fe phase inside the sample.

3.3 Reaction mechanisms

There are two different stable iron silicide phases at room temperature [31], $\alpha\text{-FeSi}$ and $\beta\text{-FeSi}_2$, both of which have very good mechanical properties with microhardness around 900 HV and 574 HV [32], respectively. In this study, we successfully generated micro-sized

Fe-Si intermetallic phases by liquid metallurgy for the first time. In the Zn-3Fe-1Si sample, FeSi₂ and Zn-Fe intermetallic phase Fe₁₁Zn₄₀ were generated, based on the EDS point scanning and XRD analysis. In comparison, with the addition of more Fe and Si, two different Fe-Si intermetallic phases, FeSi and Fe₅Si₃, were generated in the Zn-6Fe-6Si sample. However, there was no Zn-Fe phase observed in the Zn-6Fe-6Si sample. It suggests that the following reactions are favorable in the ternary alloy system when holding at 825°C.



At first, the chemical reaction occurs according to equation 1, and FeSi₂ phase is generated when Si powders are added to the alloy melt. Because of the limited supply of Si in the system, the reaction was not complete. Residual Zn-Fe phases as well as Si particles were observed in Fig. 2 and Fig. 3. With the increase of Fe to Si ratio, the reaction shown in equation 1 finished and potential subsequent reactions occurred as proposed in equations 2, 3, and 4 (See Fig. 2 and Fig. 3). During this period, FeSi and Fe₅Si₃ co-existed, while the FeSi₂ intermetallic phase was consumed [33].

These proposed reactions are feasible, given the favorable Gibbs free energy change. The Gibbs free energy of Fe₁₁Zn₄₀ was estimated to be -3.1 kJ/mol based on Ref. [34]. The Gibbs free energy of FeSi₂ and FeSi were obtained from the standard thermodynamic values table in Ref. [35] (i.e., $G_{\text{FeSi}_2} = -78.2 \text{ kJ/mol}$ and $G_{\text{FeSi}} = -78.6 \text{ kJ/mol}$). The Gibbs free energy of Fe₅Si₃ was estimated to be -285.2 kJ/mol [36]. Using the abovementioned data, the Gibbs free energy difference of each reaction was calculated. For reaction 1, $G_1 = -857.1 \text{ kJ/mol}$. For reaction 2, $G_2 = -865.9 \text{ kJ/mol}$. For reaction 3, $G_3 = -3658.9 \text{ kJ/mol}$. For reaction 4, $G_4 = -537.2 \text{ kJ/mol}$. These negative Gibbs free energy changes support the proposed chemical reactions (equations 1-4).

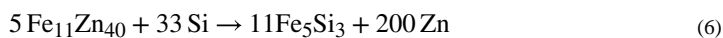
With this understanding, Fig. 4 was plotted to illustrate the energy change during holding. Each bolded black horizontal line represents the Gibbs free energy of each involving matter.

G represents the Gibbs free energy difference in each reaction. $K_B T_{\text{processing}}$ is the thermal energy provided during holding, where K_B is the Boltzmann constant and $T_{\text{processing}}$ is the holding temperature. The following conclusions can be made based on the above-mentioned calculations:

1. In sample 1 (Zn-3Fe-1Si), reaction 1 occurred spontaneously because $G_1 < 0$. Also, the thermal energy $K_B T_{\text{processing}}$ was large enough to overcome the energy barrier caused by the interfacial energy increase during the reaction (shown in Fig. 4, red line). As the reaction continued, with more Si inside the system,

enough accumulation of FeSi₂ triggered reaction 2 (shown in Fig. 4, green line) and reaction 4 (shown in Fig. 4, yellow line).

2. Given the large Gibbs free energy difference between FeSi₂ and Fe₅Si₃, reaction 2 (shown in Fig. 4, green line) could further proceed via reaction 3 (shown in Fig. 4, blue line) to produce Fe₅Si₃. Since FeSi is generated and consumed simultaneously via reaction 2 (shown in Fig. 4, green line) and reaction 3 (shown in Fig. 4, blue line), given the dynamic equilibrium in the system, residual FeSi should be expected (as shown in Fig. 3)
3. The XRD result of only FeSi₂ in the Zn-3Fe-1Si sample (see Fig. 3) indicates that Fe₁₁Zn₄₀ cannot directly transit to either FeSi or Fe₅Si₃, and the following reaction 5 and reaction 6 cannot happen under the designed reaction conditions. Although G are negative for both reactions, the thermal energy cannot supply the activation energy to trigger these reactions effectively (shown in Fig. 4, black dash lines).



Like other ternary systems such as Ti-Al-Si [37] and Cu-Ni-Si [38], Si-rich phases can be stabilized and tune other intermetallic phases during the reaction and processing.

3.4 Mechanical properties

Knowing the reaction mechanism and being able to quantitatively tune the alloy concentration and phases, we further measured the alloy properties to assess the suitability of Zn-Fe-Si as a biodegradable metal for various implant applications. The Vickers microhardness for as-cast pure Zn was 34.9±1.2 [23]. It was 41.0 ± 6.8 and 50.1 ± 6.7 HV for Zn-3Fe-1Si and Zn-6Fe-6Si samples, respectively (Fig. 5). ANOVA testing for microhardness returned a p-value of 0.026, indicating that statistically significant amounts of variance exist between the three groups tested. It is worth mentioning that the microhardness is higher in the Fe-Si phase-rich area than in the zinc-rich region, which caused a relatively high standard deviation in the hardness results.

Tensile testing was performed after hot rolling. Standard subsize dog bone shape tensile bars are shown in the inserted image of Fig. 6. Compared with pure Zn, the yield strength (YS) of Zn-3Fe-1Si sample increased by 179% from 35.6 MPa [23] to 99.6 MPa. The ultimate tensile strength (UTS) also increased by 76% from 89.1 MPa [23] to 156.5 MPa, while the ductility decreased from 70% to 40% (Fig. 6). For the Zn-6Fe-6Si sample, the YS increased by 144% from 35.6 MPa to 86.7 MPa, and the UTS also increased by 50% from 89.1 MPa to 133.6 MPa, with ductility of 30%. Statistical testing showed p-values for YS, UTS, and ductility variance as 0.00039, 0.00068, and 0.0015 respectively. In brief, for all mechanical properties, the null hypothesis was rejected, so compositionally induced differences are statistically significant.

The successful synthesis of micro-sized Fe-Si intermetallic phases within the Zn matrix improved the mechanical properties of the Zn-Fe-Si samples compared to pure Zn. More specifically, the intermetallic phases enhanced the mechanical properties via Orowan strengthening where the microphase blocked dislocation motion [39]. Compare to Zn-Fe alloys that contain large brittle Zn-Fe intermetallic phases and usually have bad ductility [20], the addition of Si tuned the Zn-Fe phases via reaction, resulting in a favorable elongation to failure that was higher than 30%.

3.5 Toxicity analysis by indirect cytotoxicity test

Cell viability was measured using the MTT assay, which uses cellular metabolic activity as an indicator of cell viability. On day 1, HUVECs exposed to Zn-3Fe-1Si extract showed greater viability than those cells exposed to Zn-6Fe-6Si extracts (Fig. 7, $P=0.0007$). Statistical analysis also showed that there was no significant difference ($P=0.0535$) between the control cells and cells exposed to Zn-3Fe-1Si extract while there was a significant difference in viability between the control cells and the cells exposed to Zn-6Fe-6Si extract ($P<0.0001$). However, by day 3, there was no significant difference in cell viability between the samples and the control group. Statistical testing showed p-values as high as 0.6341 (between the control group and Zn-3Fe-1Si) and 0.9884 (between the control group and Zn-6Fe-6Si), respectively.

The initial toxicity to HUVEC cells increased with increasing Fe and Si atomic percentages. The exact mechanism behind the initial toxicity of the Zn-6Fe-6Si sample was not studied here. However, as seen in Fig. 2, the increased density of Fe-Si intermetallic phases within the Zn matrix and additional alloying elements changed the chemical composition and structure of the metal surface. This heterogeneity creates localized regions that can act as cathodes and anodes, which promote corrosion and can lead to corrosion rates that are significantly different from the pure metal as well as between alloys with the same constituents but at different concentrations [20][40][41]. Oxides of all three metals have previously been shown to have a dose-dependent impact on cell viability [42][43][44]. Despite the toxicity of the Zn-6Fe-6Si extract to HUVECs on day 1, the cell viability levels rebounded by day 3. This initial investigation into the biocompatibility of Zn-Fe-Si as a possible BRS material is promising, but additional studies are required (e.g. genotoxicity and hemocompatibility) to fully answer whether Zn-Fe-Si alloys are appropriate for this clinical application. Furthermore, current cytotoxicity standards were designed with non-degradable metals in mind and fail to account for in vivo clearance mechanisms (e.g., circulation) that would prevent the accumulation of degradation products [45][46]. As such, the doses of soluble degradation products the cells were exposed to may be exaggerated even with the dilution factor used in this study.

3.6 Corrosion behavior

To determine whether there was a difference in the corrosion behavior between the two alloys and pure Zn, a 2-week immersion study of the Zn-Fe-Si alloys in a 0.9% w/v NaCl solution was performed, and the ion concentrations for Zn, Fe, and Si in the immersion solution were measured via ICP-MS. There was no statistically significant difference in cumulative Zn ion release between the pure Zn and the two alloys at any of the time points

(Fig. 8). Using ASTM G31 standard and the immersion results, the corrosion rates (Table 2) were calculated according to equation (7):

$$CR = (K \times m) / (A \times t \times \rho) \quad (7)$$

where K is the CR constant 8.76×10^4 , m is mass loss (g), A is exposed surface area (cm^2), t is time (h), and ρ is the density (g/cm^3). The densities of the alloys were calculated using the mixture rule. These results suggest Zn-Fe-Si alloys have a corrosion rate similar to pure Zn and should satisfy the degradation rate criteria of <0.02 mm/yr for BRS as well as other biomedical applications where the Zn corrosion rate is ideal. Little-to-no Fe ions were detected in the immersion solution during the 2-week study. Two of the Zn-3Fe-1Si samples had quantifiable Fe ion concentrations during the study with cumulative Fe release on day 14 of 0.77 ng/ mm^2 (± 0.11 ; $n=2$). All other samples had Fe ion concentrations below the detection limit throughout the immersion study (Fe detection limit = 0.49 ppb). The Zn-6Fe-6Si samples had a cumulative Fe release at day 14 of 1.52 ng/ mm^2 (± 0.92 ; $n=5$) with only one sample having Fe ion concentrations below the detection limit throughout the study. There were no Si ions detected in the immersion solution of the Zn-Fe-Si alloys until day 14; however, only 4 of the Zn-3Fe-1Si samples had trace ion levels that were below the detection limit (Si detection limit = 1.95 ppb). One of the Zn-6Fe-6Si samples had quantifiable levels of released Si (16.06 ng/ mm^2) while the remaining samples had Si ion concentrations below the detection limit. It has been previously reported that iron-silicides have good corrosion resistance in NaCl solution [47], and this would explain the limited quantities detected during this study. In general, *in vitro* corrosion tests do not fully reflect the corrosive environment medical implants are exposed to during *in vivo* use. Furthermore, corrosion rates predicted from *in vitro* data are based on results obtained over a much shorter time scale. Taken altogether, it is not unusual for corrosion rates calculated from *in vitro* data versus *in vivo* data can be an order of magnitude different [48][49]. *In vivo* studies on the Zn-Fe-Si alloys will be required to assess their corrosion rates more accurately.

Overall, the suitability of this material as a potential candidate for biodegradable implant applications and specifically for BRS applications is promising. Compared to other current biodegradable Zn alloys that undergo hot rolling processing [19][22][50][51], the Zn-Fe-Si alloy reported in this study showed significant improvement in ductility (Fig. 9), which is very important for BRS applications since stents need to expand during deployment. Additionally, the fairly low yield strength is important for loading the stent onto balloon catheters via stent crimping, and allowing for stent expansion using low pressures during deployment. However, the UTS for the Zn-Fe-Si alloys reported in this study fall below the target of >250 MPa UTS for BRS applications. This is an important metric for stent materials since it is directly proportional to radial strength and allows for thin strut design (i.e., low profile). Encouragingly, the ductility of the alloys remained $>30\%$. Composition tuning and post processing, such as hot extrusion, could further improve the strength such that all mechanical benchmark values for BRS materials [52] are satisfied. Furthermore, the Zn-Fe-Si alloys are expected to be thermally stable since Fe-Si phases have high melting temperatures. Compared to other Zn alloys that have historically used low-melting-temperature Zn-X phases for strengthening [53], the Zn-Fe-Si alloys in this study should

have a longer shelf life and retain their mechanical properties during storage, implantation, and service. This hypothesis needs to be investigated in future studies.

4 CONCLUSION

This study introduced micro-sized Fe-Si intermetallic phases into the Zn matrix using a liquid metallurgy method. The formation and interconversion of different Fe-Si intermetallic phases were confirmed using SEM, XRD, and Gibbs free energy analysis. Evaluation of the mechanical properties showed that the microhardness and tensile strength of the Zn-Fe-Si alloys significantly increased when compared to pure Zn because of Orowan strengthening while the ductility was maintained above 30% by controlling the volume of the large brittle Zn-Fe phases. Furthermore, the indirect cytotoxicity test showed that the biocompatibility of this novel alloy is acceptable. A 2-week immersion study showed the corrosion rate of Zn-Fe-Si alloys were similar to pure Zn. The combination of favorable mechanical properties, biocompatibility, and corrosion rate makes this novel material a promising candidate as a BRS metal. Future studies aimed at producing denser sub-micron-sized Fe-Si intermetallic phases should further enhance the mechanical performance. Additionally, the long-term corrosion and anti-aging behavior of the Zn-Fe-Si alloys requires investigation.

ACKNOWLEDGEMENTS

The research reported in this publication was supported by the National Heart, Lung, and Blood Institute (NHLBI) of the National Institutes of Health (NIH) under award number R01 HL143465. The content is solely the responsibility of the authors and does not necessarily represent the official views of the NIH. The authors acknowledge Dr. Chong Hyun (Paul) Chang, University of California Center for Environmental Implications of Nanotechnology (UC-CEIN), University of California, Los Angeles (UCLA), for his help with the ICP-MS data acquisition. The author also acknowledges Mr. Narayanan Murali at UCLA for his help in data analysis.

DATA AVAILABILITY

The datasets generated during and/or analyzed during the current study are not publicly available because it belongs to ongoing research. It could be available from the corresponding author on reasonable request.

REFERENCES

- [1]. Li C et al. (2020) Design of biodegradable, implantable devices towards clinical translation. *Nature Reviews Materials*, 5: 61–81.
- [2]. Niccoli Giampaolo, Montone Rocco A., Ferrante Giuseppe, Crea Filippo, The Evolving Role of Inflammatory Biomarkers in Risk Assessment After Stent Implantation, *J Am Coll Cardiol*. 2010 Nov, 56 (22) 1783–1793. [PubMed: 21087705]
- [3]. Rittersma SZH, et al. (2004) Impact of strut thickness on late luminal loss after coronary artery stent placement. *The American Journal of Cardiology*, 93(4): 477–480. [PubMed: 14969629]
- [4]. Learmonth ID, et al. (2007) The operation of the century: total hip replacement. *The Lancet*, 370(9597): 1508–1519.
- [5]. Li Huafang, Zheng Yufeng, Qin Ling, Progress of biodegradable metals, *Progress in Natural Science: Materials International*, Volume 24, Issue 5, 2014, Pages 414–422, ISSN 1002-0071, 10.1016/j.pnsc.2014.08.014.
- [6]. Kenny D, & Hijazi ZM, Bioresorbable stents for pediatric practice: where are we now? *Interventional Cardiology*, 2015, 7(3), 245–255. doi:10.2217/ica.15.6

- [7]. Verheye S, et al. (2020) BIOSOLVE-IV-registry: Safety and performance of the Magmaris scaffold: 12-month outcomes of the first cohort of 1,075 patients. *Catheterization & Clinical Interventions*.
- [8]. Haude M et al. (2013) Safety and performance of the drug-eluting absorbable metal scaffold (DREAMS) in patients with de-novo coronary lesions: 12 month results of the prospective, multicentre, first-in-man BIOSOLVE-I trial. *Lancet North Am. Ed* 381(9869): 836–844
- [9]. Haude M et al. (2016) Safety and performance of the DRug-Eluting Absorbable Metal Scaffold (DREAMS) in patients with de novo coronary lesions: 3-year results of the prospective, multicentre, first-in-man BIOSOLVE-I trial. *J Eurointervention*. 12(2): e160–e166.
- [10]. Haude M, et al. (2016) Safety and performance of the second-generation drug-eluting absorbable metal scaffold in patients with de-novo coronary artery lesions (BIOSOLVE-II): 6 month results of a prospective, multicentre, non-randomised, first-in-man trial. *Lancet North Am. Ed* 387(10013): 31–39.
- [11]. Garcia-Garcia HM, et al. (2018) In vivo serial invasive imaging of the second-generation drug-eluting absorbable metal scaffold (Magmaris—DREAMS 2G) in de novo coronary lesions: insights from the BIOSOLVE-II first-in-man trial. *Int. J. Cardiol* 255: 22–28. [PubMed: 29292064]
- [12]. Sezer Nurettin, Evis Zafer, Kayhan Said Murat, Tahmasebifar Aydin, Koç Muammer, Review of magnesium-based biomaterials and their applications, *Journal of Magnesium and Alloys*, Volume 6, Issue 1, 2018, Pages 23–43, ISSN 2213-9567, 10.1016/j.jma.2018.02.003.
- [13]. Noviana Deni, Paramitha Devi, Ulum Mokhammad Fakhrol, Hermawan Hendra, The effect of hydrogen gas evolution of magnesium implant on the postimplantation mortality of rats, *Journal of Orthopaedic Translation*, Volume 5, 2016, Pages 9–15, ISSN 2214-031X, 10.1016/j.jot.2015.08.003. [PubMed: 30035070]
- [14]. Oliver AA, et al. (2021) Recent advances and directions in the development of bioresorbable metallic cardiovascular stents: Insights from recent human and in vivo studies. *Acta Biomaterialia*. 127: 1–23. [PubMed: 33823325]
- [15]. Moravej M, Mantovani D. Biodegradable Metals for Cardiovascular Stent Application: Interests and New Opportunities. *International Journal of Molecular Sciences*. 2011; 12(7):4250–4270. [PubMed: 21845076]
- [16]. Fagali Natalia S., Grillo Claudia A., Puntarulo Susana, Fernández Mónica A. de Mele Lorenzo, Cytotoxicity of corrosion products of degradable Fe-based stents: Relevance of pH and insoluble products, *Colloids and Surfaces B: Biointerfaces*, Volume 128, 2015, Pages 480–488, ISSN 0927-7765, 10.1016/j.colsurfb.2015.02.047. [PubMed: 25797480]
- [17]. Zheng JF, et al. (2019) Preclinical evaluation of a novel sirolimus-eluting iron bioresorbable coronary scaffold in porcine coronary artery at 6 months. *JACC: Cardiovascular Interventions*, 12(3): 245–255. [PubMed: 30732729]
- [18]. Bowen PK, Drelich J and Goldman J (2013), Zinc Exhibits Ideal Physiological Corrosion Behavior for Bioabsorbable Stents. *Adv. Mater*, 25: 2577–2582. doi:10.1002/adma.201300226 [PubMed: 23495090]
- [19]. Bowen PK, Seitz J-M, Guillory RJ II, Braykovich JP, Zhao S, Goldman J, Drelich JW. 2018. Evaluation of wrought Zn–Al alloys (1, 3, and 5 wt % Al) through mechanical and in vivo testing for stent applications. *J Biomed Mater Res Part B* 2018: 106B: 245–258.
- [20]. Kafri A, Ovadia S, Goldman J, Drelich J, Aghion E. The Suitability of Zn–1.3%Fe Alloy as a Biodegradable Implant Material. *Metals*. 2018; 8(3):153.
- [21]. Liu Xiwei, Sun Jianke, Qiu Kejin, Yang Yinghong, Pu Zhongjie, Li Li, Zheng Yufeng, Effects of alloying elements (Ca and Sr) on microstructure, mechanical property and in vitro corrosion behavior of biodegradable Zn–1.5Mg alloy, *Journal of Alloys and Compounds*, Volume 664, 2016, Pages 444–452, ISSN 0925-8388, 10.1016/j.jallcom.2015.10.116.
- [22]. Li H, Xie X, Zheng Y et al. Development of biodegradable Zn-1X binary alloys with nutrient alloying elements Mg, Ca and Sr. *Sci Rep* 5, 10719 (2015). 10.1038/srep10719 [PubMed: 26023878]
- [23]. Guan Z, Pan S, Linsley C, Li X. Manufacturing and Characterization of Zn-WC as Potential Biodegradable Material, *Procedia Manufacturing*, 34 (2019), pp. 247–251 [PubMed: 34007864]

- [24]. Guan Z, et al. (2020) Novel Zinc / Tungsten Carbide Nanocomposite as Bioabsorbable Implant. *Materials Letters*. 263: 127282. [PubMed: 32647402]
- [25]. Guan Z et al. (2020) Highly Ductile Zn-2Fe-WC Nanocomposite as Biodegradable Material. *Metall Mater Trans A*, 51, 4406–4413.
- [26]. Pan S, Jin K, Wang T et al. Metal matrix nanocomposites in tribology: Manufacturing, performance, and mechanisms. *Friction* (2022). 10.1007/s40544-021-0572-7
- [27]. Guan Z, Linsley CS, Pan S, et al. Zn–Mg–WC Nanocomposites for Bioresorbable Cardiovascular Stents: Microstructure, Mechanical Properties, Fatigue, Shelf Life, and Corrosion[J]. *ACS Biomaterials Science & Engineering*, 2021.
- [28]. Abbaspour N, et al. (2014) Review on iron and its importance for human health. *J Res Med Sci*. 19(2): 164–174. [PubMed: 24778671]
- [29]. Jugdaohsingh R (2007) Silicon and bone health. *J Nutr Health Aging*. 11(2): 99–110. [PubMed: 17435952]
- [30]. Su Xuping, Tang Nai-Yong & Toguri Jim M. (2001) 450 °C Isothermal Section of the Fe-Zn-Si Ternary Phase Diagram, *Canadian Metallurgical Quarterly*, 40:3, 377–384, DOI: 10.1179/cm.2001.40.3.377
- [31]. Dézsi I, Fetzler Cs, Sz cs I, Dekoster J, Vantomme A, Caymax M, Stable and metastable iron silicide phases on Si(100), *Surface Science*, Volume 599, Issues 1–3, 2005, Pages 122–127, ISSN 0039–6028, 10.1016/j.susc.2005.09.040.
- [32]. Milekhine V, Onsøien MI, Solberg JK and Skaland T: ‘Mechanical properties of FeSi (ε), FeSi₂ (ζα) and Mg₂Si’, *Intermetallics*, 2002, 10, 743–750. doi: 10.1016/S0966-9795(02)00046-8
- [33]. Zhi-shui YU, Rui-feng LI, Kai QI, Growth behavior of interfacial compounds in galvanized steel joints with CuSi₃ filler under arc brazing, *Transactions of Nonferrous Metals Society of China*, Volume 16, Issue 6, 2006, Pages 1391–1396, ISSN 1003–6326, 10.1016/S1003-6326(07)60026-0.
- [34]. Petersen Stephan, Spencer Philip J., Hack Klaus, A thermodynamic evaluation of the iron-zinc system, *Thermochimica Acta*, Volume 129, Issue 1, 1988, Pages 77–87, ISSN 0040–6031, 10.1016/0040-6031(88)87199-5.
- [35]. Standard Thermodynamic Values, <https://www.drjez.com/uco/ChemTools/Standard%20Thermodynamic%20Values.pdf>
- [36]. Basak S, Pal TK, Shome M, and Maity J. "GMA brazing of galvanized interstitial-free steel." *Welding journal* 92, no. 2 (2013): S29–S35
- [37]. Cabibbo M, et al. "Role of Si on lamellar formation and mechanical response of two SPS Ti–15Al–15Si and Ti–10Al–20Si intermetallic alloys." *Intermetallics* 131 (2021): 107099.
- [38]. Li Jiang, et al. "Effect of Ni/Si mass ratio and thermomechanical treatment on the microstructure and properties of Cu-Ni-Si alloys." *Materials* 12.13 (2019): 2076.
- [39]. Zhang Z, Chen DL, Contribution of Orowan strengthening effect in particulate-reinforced metal matrix nanocomposites, *Materials Science and Engineering: A*, Volumes 483–484, 2008, Pages 148–152, ISSN 0921–5093, 10.1016/j.msea.2006.10.184.
- [40]. Liu LM, Gebresellase K, Collins B, Zhang HL, Xu ZG, Sankar J, et al. Degradation Rates of Pure Zinc, Magnesium, and Magnesium Alloys Measured by Volume Loss, Mass Loss, and Hydrogen Evolution. *Appl Sci-Basel*. 2018;8(9).
- [41]. Kabir H, Munir K, Wen C, Li YC. Recent research and progress of biodegradable zinc alloys and composites for biomedical applications: Biomechanical and biocorrosion perspectives. *Bioact Mater*. 2021;6(3):836–79. [PubMed: 33024903]
- [42]. Wu X, et al. (2010) Toxic effects of iron oxide nanoparticles on human umbilical vein endothelial cells. *Int J Nanomedicine*, 5: 385–399. [PubMed: 20957160]
- [43]. Poier N, et al. (2020) Effects of Zinc Oxide Nanoparticles in HUVEC: Cyto- and Genotoxicity and Functional Impairment After Long-Term and Repetitive Exposure in vitro. *Int J Nanomedicine*, 15: 4441–4452. [PubMed: 32606688]
- [44]. Duan J, et al. (2013) Toxic Effect of Silica Nanoparticles on Endothelial Cells through DNA Damage Response via Chk1-Dependent G2/M Checkpoint. *PLoS One*, 8(4): e62087. [PubMed: 23620807]

- [45]. Wang J, et al. Recommendation for modifying current cytotoxicity testing standards for biodegradable magnesium-based materials. *Acta Biomaterialia* 2015, 21, 237–249. [PubMed: 25890098]
- [46]. Jablonská E, et al. Test conditions can significantly affect the results of in vitro cytotoxicity testing of degradable metallic biomaterials. *Scientific Reports* 2021, 11, 6628. [PubMed: 33758226]
- [47]. Kwok CT, et al. Laser surface modification of UNS S31603 stainless steel. Part I: microstructures and corrosion characteristics. *Materials Science and Engineering: A* 2000, 290(1–2), 55–73.
- [48]. Chen K, et al. In vitro and in vivo degradation behavior of Mg–2Sr–Ca and Mg–2Sr–Zn alloys. *Bioactive Materials* 2020, 5(2), 275–285. [PubMed: 32128466]
- [49]. Sanchez AHM, et al. Mg and Mg alloys: how comparable are in vitro and in vivo corrosion rates? A review. *Acta Biomaterialia* 2015, 13, 16–31. [PubMed: 25484334]
- [50]. Li H, Yang H, Zheng Y, et al. Design and characterizations of novel biodegradable ternary Zn-based alloys with IIA nutrient alloying elements Mg, Ca and Sr[J]. *Materials & Design*, 2015, 83: 95–102.
- [51]. Shi ZZ, Yu J, Liu XF, et al. Fabrication and characterization of novel biodegradable Zn-Mn-Cu alloys[J]. *Journal of materials science & technology*, 2018, 34(6): 1008–1015.
- [52]. Mostaed E, et al. (2018) Zinc-based alloys for degradable vascular stent applications. *Acta Biomaterialia*, 71: 1–23. [PubMed: 29530821]
- [53]. Jin H; Zhao S; Guillory R; Bowen PK; Yin Z; Griebel A; Schaffer J; Earley EJ; Goldman J; Drelich JW Novel high-strength, low-alloys Zn-Mg (< 0.1 wt% Mg) and their arterial biodegradation. *Mater. Sci. Eng., C* 2018, 84, 67–79, DOI: 10.1016/j.msec.2017.11.021

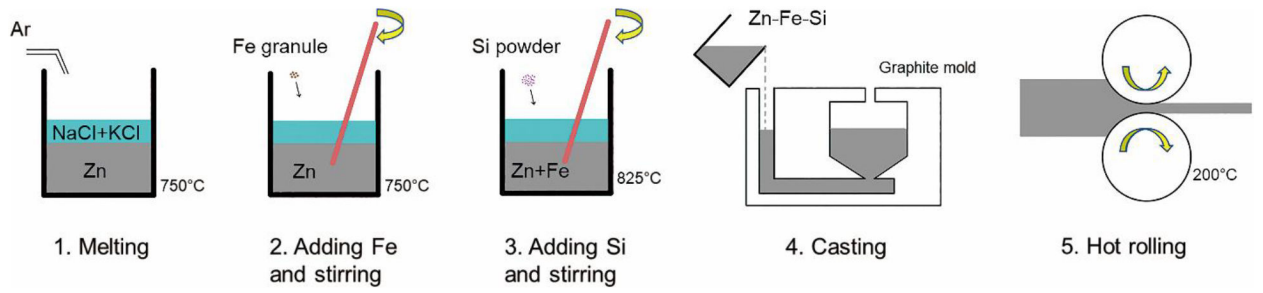


Fig. 1.
Schematic diagram of the Zn-Fe-Si fabrication process

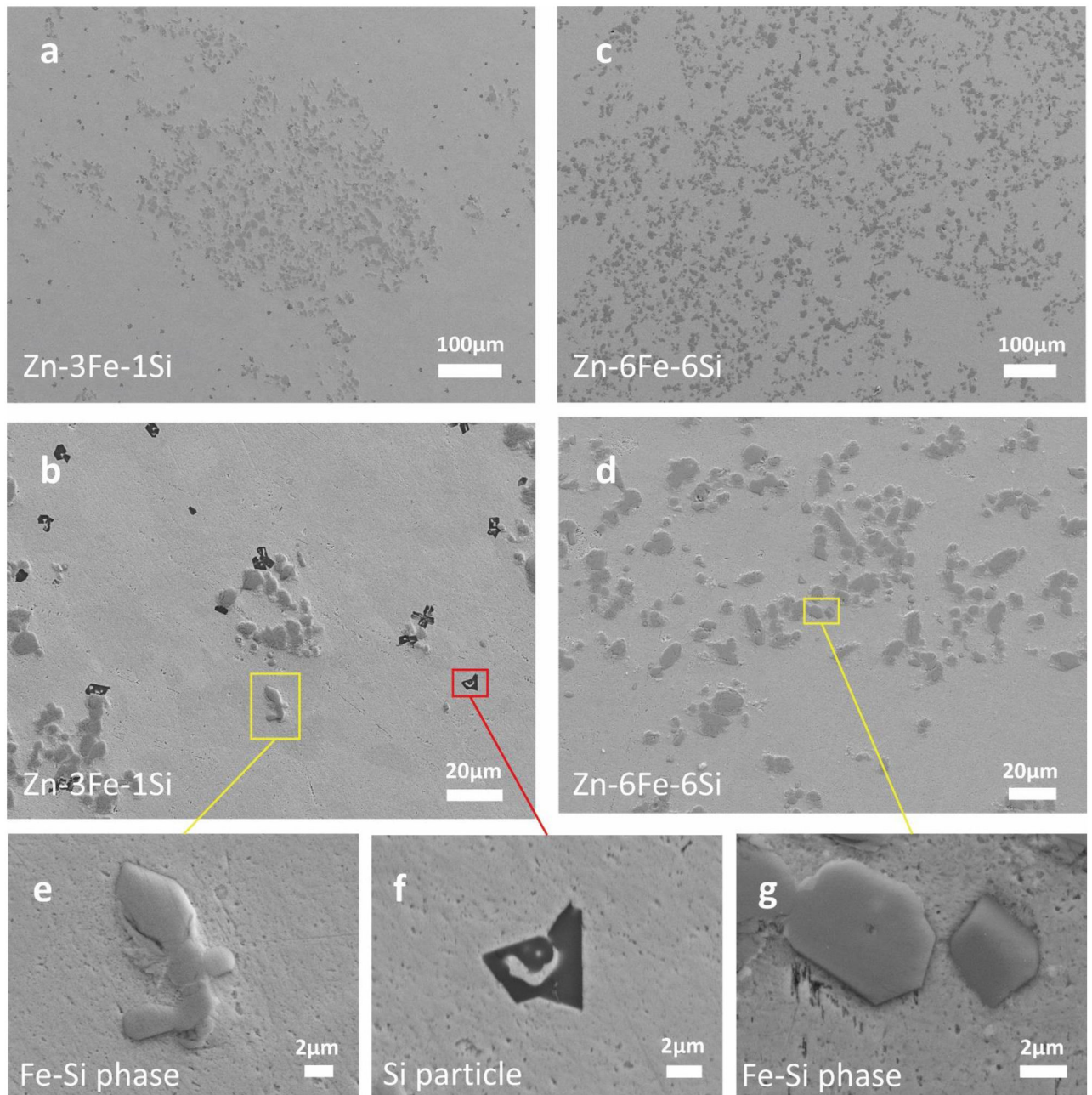


Fig. 2. SEM images of Zn-Fe-Si alloys with different compositions. (a) and (b) represent the Zn-3Fe-1Si sample. (c) and (d) represent the Zn-6Fe-6Si sample. (e) and (f) are the magnified images of Fe-Si phase and Si particle present in the Zn-3Fe-1Si sample, respectively, and (g) is the magnified images of Fe-Si intermetallic phase in the Zn-6Fe-6Si sample

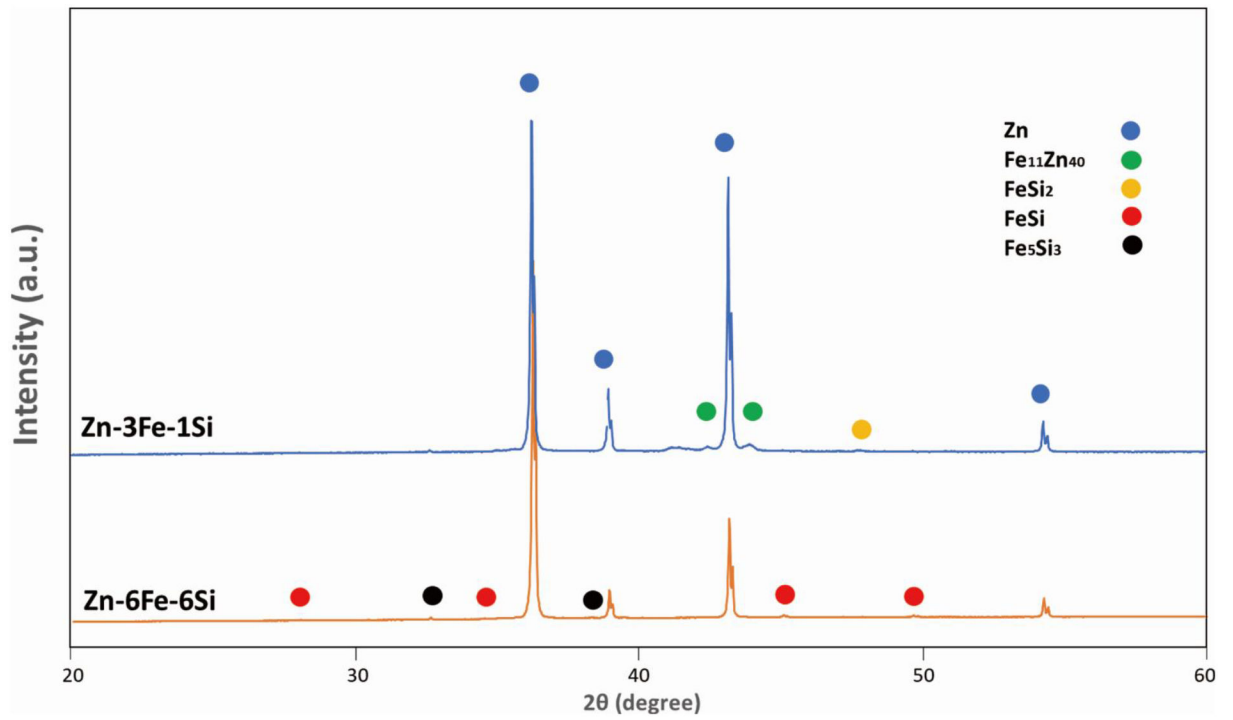


Fig. 3.
Diffraction patterns of Zn-3Fe-1Si (blue line) and Zn-6Fe-6Si (orange line) samples

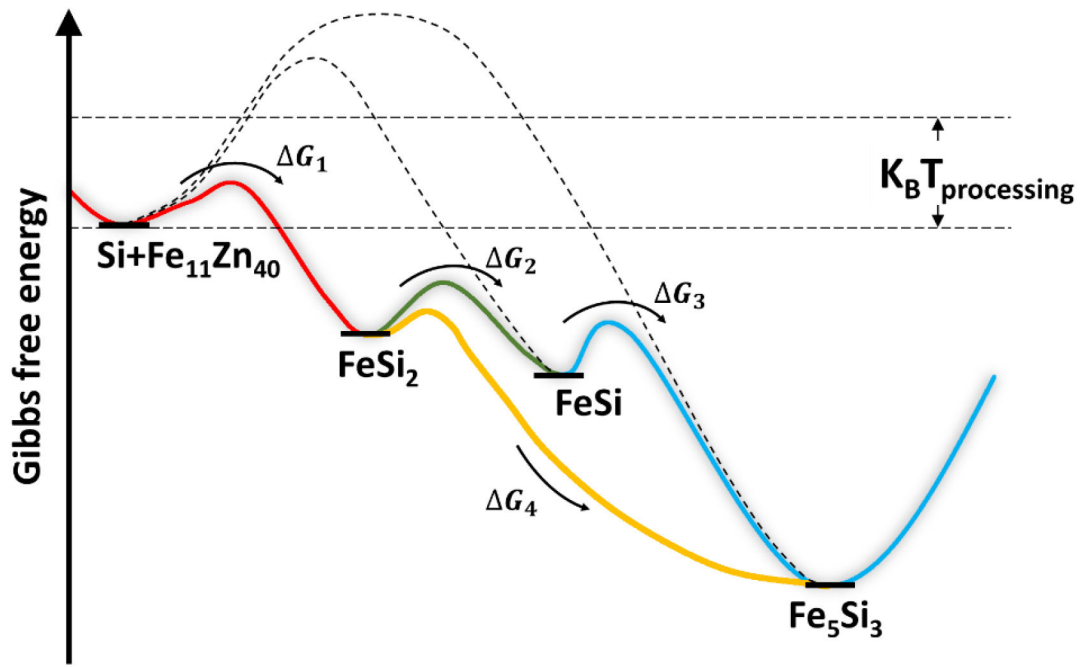


Fig. 4.
Gibbs free energy analysis during the isothermal reaction at 825 °C

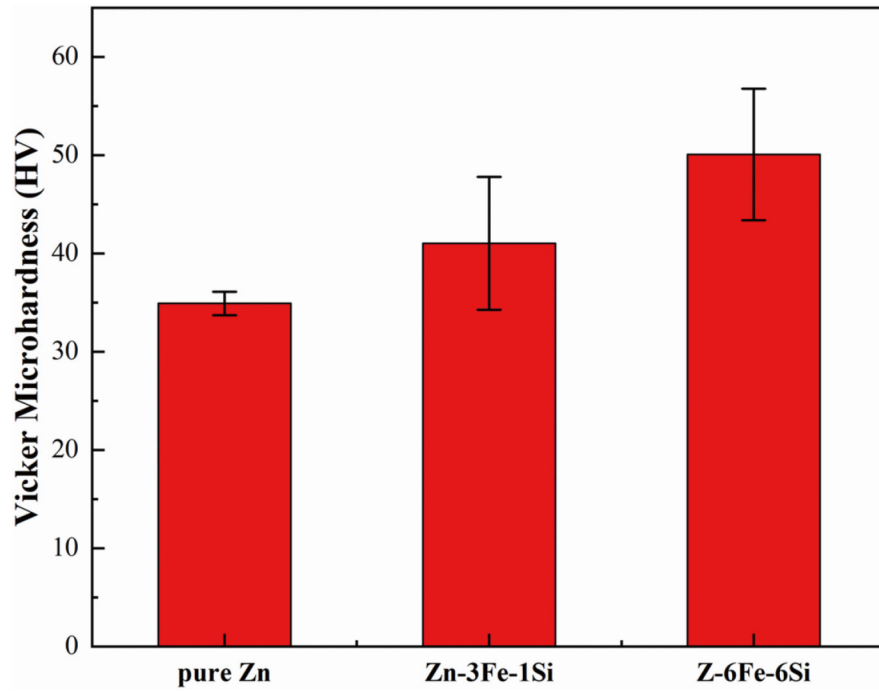


Fig. 5. Vickers microhardness of pure Zn and Zn-Fe-Si samples (n=8)

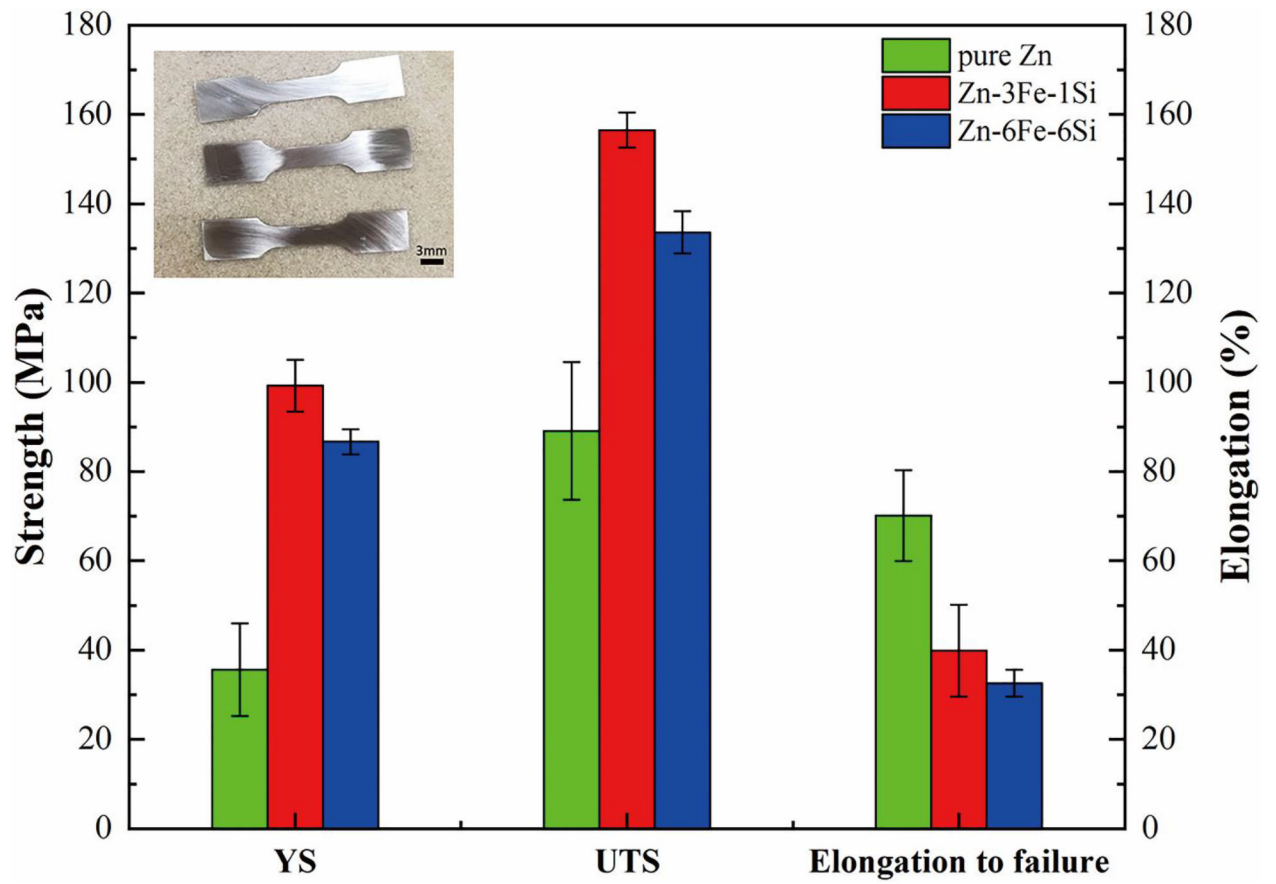


Fig. 6. Tensile properties of pure Zn [23] and Zn-Fe-Si alloys (n=4)

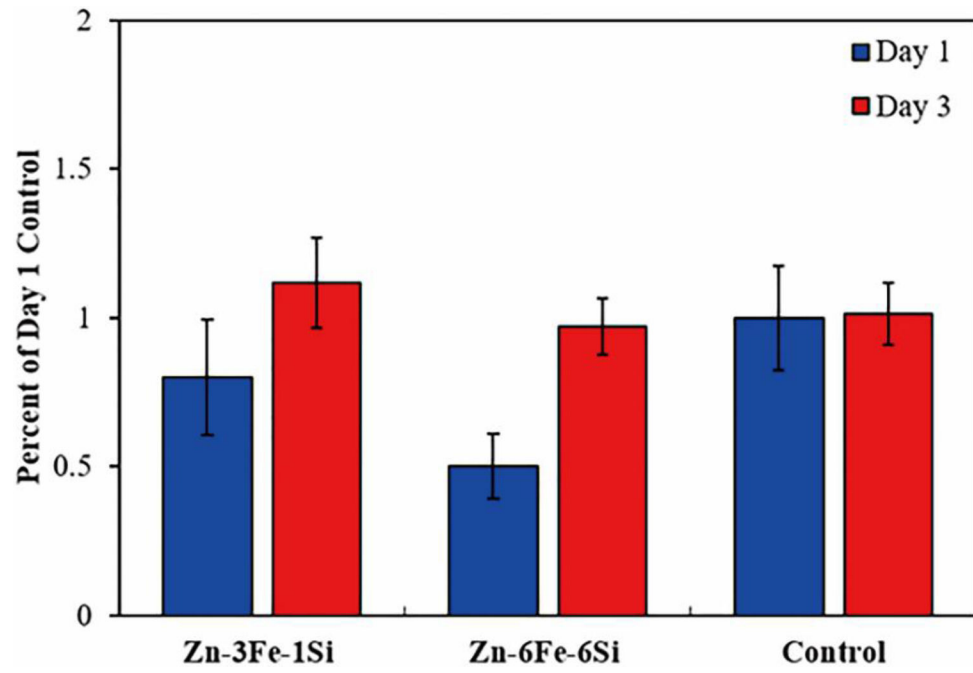


Fig. 7. HUVEC viability is shown as the percentage of viable cells in the day 1 control group after 1 and 3 days of culture in medium containing extract of the Zn-Fe-Si samples (n = 9)

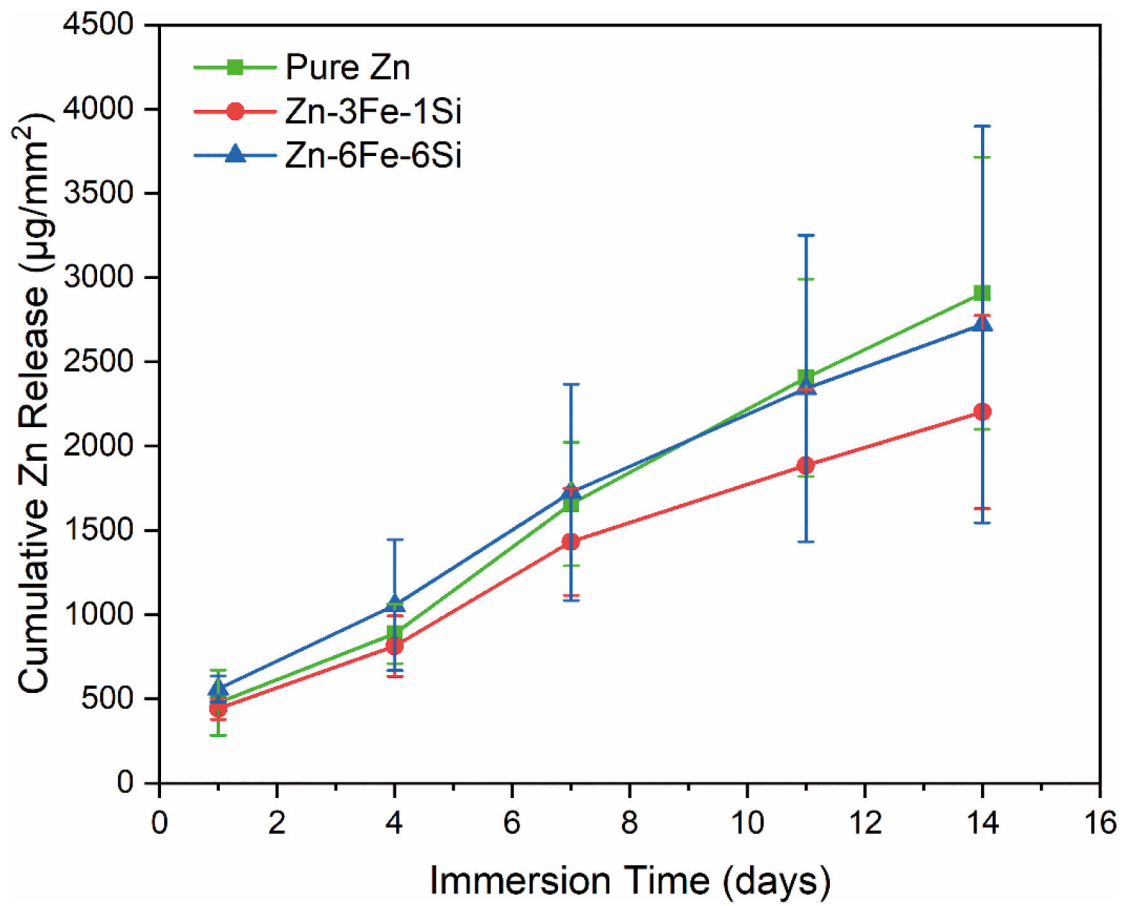


Fig. 8. Cumulative Zn ion release during a 2-week immersion test in a 0.9% w/v NaCl solution at 37 °C (n=6). Both alloys showed a similar corrosion rate as pure Zn manufactured using the same method

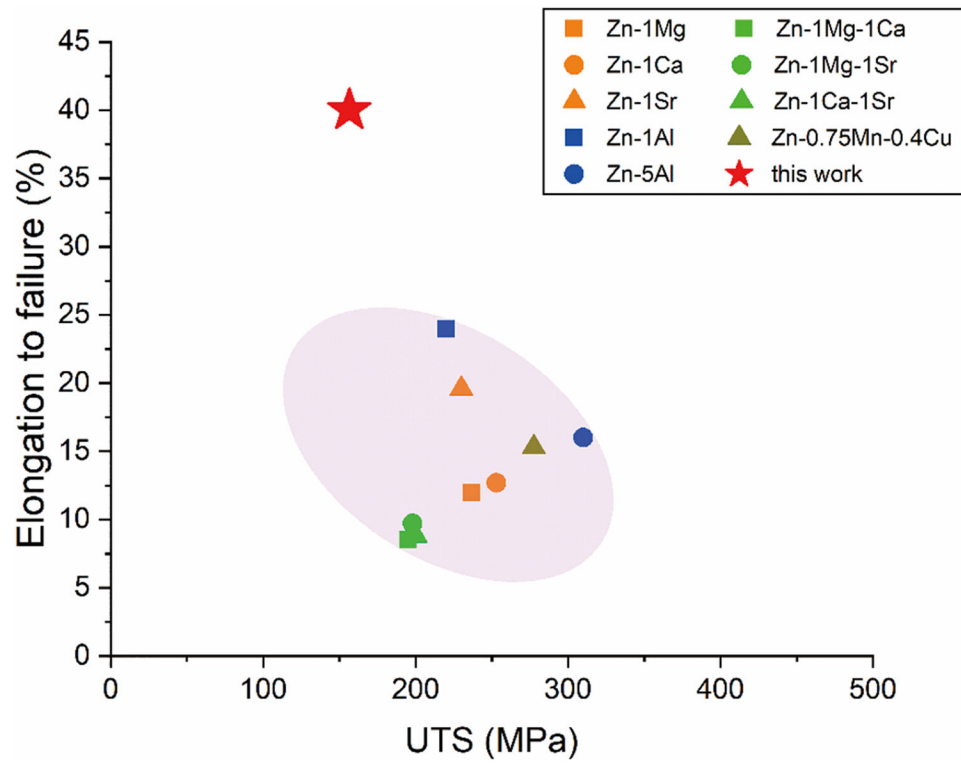


Fig. 9. Elongation to failure vs. UTS for current hot-rolled biodegradable Zn alloys [19][22][50][51]. Zn-3Fe-1Si in this study showed superior ductility. Further work such as composition tuning and post processing would help to boost the strength for BRS applications

Table 1.

ICP-MS result of Zn-Fe-Si samples with different composition

Sample	Si (at. %)	Fe (at. %)	Zn (at. %)
sample 1	1.228 ±0.014	2.723 ±0.028	Bal.
sample 2	5.566 ±0.088	6.365 ±0.065	Bal.

Author Manuscript

Author Manuscript

Author Manuscript

Author Manuscript

Table 2.

Cumulative Ion Release at Day 14 (n=6, unless otherwise noted).

Sample	Temp. (°C)	Zn (µg/mm ²)	Fe (µg/mm ²)	Si (µg/mm ²)	ρ (g/cm ³)	CR (mm/yr)
Zn	37	2.9 (±0.8)	N/A	N/A	7.133	0.014 (±0.007)
Zn-3Fe-1Si		2.2 (±0.6)	0.0008 (±0.0001) [n=2]	0.0	7.091	0.012 (±0.006)
Zn-6Fe-6Si		2.7 (±1.2)	0.0015 (±0.0009) [n=5]	0.016 [n=1]	6.794	0.016 (±0.009)

Author Manuscript

Author Manuscript

Author Manuscript

Author Manuscript